Spectral Diffusion at the Water/Lipid Interface Revealed by Two-dimensional Fourth-order Optical Spectroscopy: A Classical Simulation Study

Yuki Nagata and Shaul Mukamel

Department of Chemistry, University of California, Irvine, California 92697, USA

February 5, 2011

Supporting Information

1 Simulation Protocol

1.1 The truncated response function algorithm for computing sum-frequency generation (SFG) and IR-IR-IR-visible (IIIV) response functions

We briefly describe the truncated response function formalism developed earlier for the second-order SFG response function,[1] and extend it to the fourth-order IIIV signals. The pulse configurations for the SFG and IIIV spectroscopies are shown in Figure 1. The SFG response function is given by[2]

$$R^{(2)}_{abc}(\tau) = \frac{i}{\hbar}\mathrm{Tr}\left\{A_{ab}(t_1),[M_c(t_0),\rho]\right\}, \tag{1}$$

where $M(t_0)$ and $A(t_1)$ are the total dipole moment at time t_0 and polarizability at time t_1 of the entire system. a, b, and c represent the pulse polarization directions. $\tau = t_1 - t_0$ is the delay between the IR and visible pulses. In the classical limit, the quantum commutator can be replaced by the Poisson bracket, yielding the following classical expression for the SFG response function

$$R^{(2)}_{abc}(\tau) = -\frac{1}{k_B T}\left\langle \dot{A}_{ab}(t_1)M_c(t_0)\right\rangle. \tag{2}$$

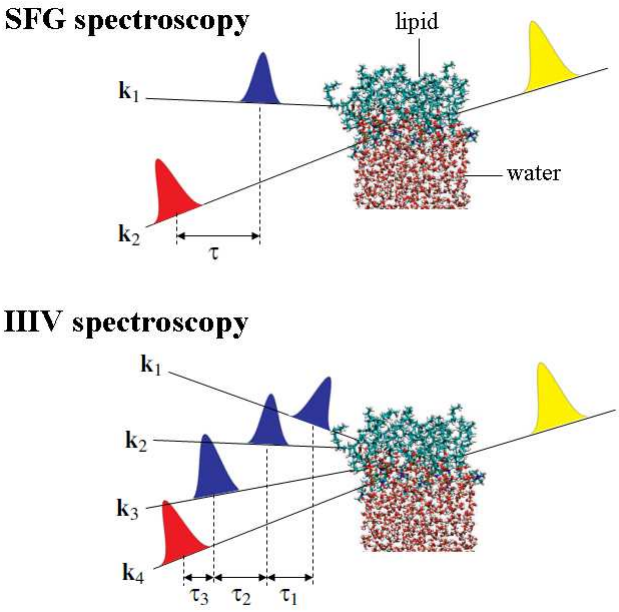

Figure 1: Pulse configurations for SFG (top) and IIIV experiments (bottom). Shown are the IR (blue), visible (red), and detection (yellow) pulses.

The total dipole moment and polarizability are given by sums of molecular dipole moments μ_i and polarizabilities α_i

$$M(t) = \sum_i \mu_i(t), \tag{3}$$

$$A(t) = \sum_i \alpha_i(t). \tag{4}$$

By inserting Equations (3) and (4) into Equation (2), we can separate it into autocorrelation and cross-correlation terms

$$R^{(2)}(\tau) = -\frac{1}{k_B T}\left(\left\langle \sum_i \dot{\alpha}_i(t_1)\mu_i(t_0)\right\rangle + \left\langle \sum_i \sum_{j(\neq i)} \dot{\alpha}_i(t_1)\mu_j(t_0)\right\rangle\right). \tag{5}$$

The two terms scale as N and N^2, respectively, where N is the number of molecules. The large fluctuations of the cross-correlation require a large number of sampling points. For faster convergence, we introduced the truncated response function which neglects the terms $\langle \dot{\alpha}_i \mu_j \rangle$ when the distance between molecules i and j is larger than a cutoff length r_t. The second-order response function (2) is recast as

$$R^{(2)}(\tau) = -\frac{1}{k_B T}\left(\left\langle \sum_i \dot{\alpha}_i(t_1)\mu_i(t_0)\right\rangle + \left\langle \sum_i \sum_{j(\neq i)} \dot{\alpha}_i(t_1)\mu_j(t_0) g_\mathrm{t}(\bar{r}_{ij}, r_\mathrm{t})\right\rangle\right), \tag{6}$$

where the truncating function is

$$g_{\rm t}(\bar{r}_{ij}, r_{\rm t}) = \begin{cases} 1 & \text{for} \quad \bar{r}_{ij} \leq r_{\rm t} \\ 0 & \text{for} \quad \bar{r}_{ij} > r_{\rm t} \end{cases}, \tag{7}$$

and $\bar{r}_{ij} = \int_{-T}^{T} dt r_{ij}(t)/2T$ is the average distance between molecules i and j.

The fourth-order response function with the IIIV pulse configuration (Figure 1) reads

$$\begin{aligned} R^{(4)}_{abcde}(\tau_3, \tau_2, \tau_1) &= \left(\frac{i}{\hbar}\right)^3 \mathrm{Tr}\left\{A_{ab}(t_3), [M_c(t_2), [M_d(t_1), [M_e(t_0), \rho]]]\right\} \\ &= \left(\frac{i}{\hbar}\right)^3 \mathrm{Tr}\left\{[A_{ab}(t_3), M_c(t_2)]\,[M_d(t_1), [M_e(t_0), \rho]]\right\}, \end{aligned} \tag{8}$$

where $t_3 = \tau_3 + \tau_2/2$, $t_2 = \tau_2/2$, $t_1 = -\tau_2/2$, $t_0 = -\tau_2/2 - \tau_1$, and a, b, c, d, e represent the pulse polarizations. In the classical limit, we replace the quantum commutations by Poission brackets and obtain

$$R^{(4)}_{abcde}(\tau_3, \tau_2, \tau_1) = -\frac{1}{k_B T}\left\langle \{A_{ab}(t_3), M_c(t_2)\}_{P.B.}\left(\frac{1}{k_B T}\dot{M}_d(t_1)\dot{M}_e(t_0) - \left\{M_d(t_1), \dot{M}_e(t_0)\right\}_{P.B.}\right)\right\rangle. \tag{9}$$

This expression may be also obtained by replacing the dipole moment at t_3 with the polarizability in the third-order response function derived by Jeon and Cho.[3] Since polarizabilities only depend on atomic positions and independent of the momenta, $\partial A/\partial p = 0$. To exploit this, we introduce the generating response function[4, 5]

$$W^{(4)}_{abcde}(\tau_3, \tau_2, \tau_1) = -\frac{1}{k_B T}\left\langle \{A_{ab}(t_3), M_c(t_2)\}_{P.B.}\left(\frac{1}{k_B T}\dot{M}_d(t_1) M_e(\tau) - \{M_d(t_1), M_e(t_0)\}_{P.B.}\right)\right\rangle, \tag{10}$$

and the fourth-order response function is finally calculated as

$$R^{(4)}(\tau_3, \tau_2, \tau_1) = -\frac{\partial}{\partial \tau_1} W^{(4)}(\tau_3, \tau_2, \tau_1). \tag{11}$$

Substituting Equations (3) and (4) into Equation (10) gives

$$\begin{aligned} W^{(4)}(\tau_3,\tau_2,\tau_1) &= -\frac{1}{k_BT}\left\langle \sum_{i,j,k,l} \{\alpha_l(t_3),\mu_k(t_2)\}_{P.B.}\left(\frac{1}{k_BT}\dot{\mu}_j(t_1)\mu_i(t_0) - \{\mu_j(t_1),\mu_i(t_0)\}_{P.B.}\right)\right\rangle \\ &= \frac{1}{k_BT}\left\langle \sum_{i,j,k,l}\left(\sum_m\sum_{a(m)} \frac{\partial\alpha_l(t_3)}{\partial \mathbf{p}_{a(m)}(t_2)}\cdot\frac{\partial\mu_k(t_2)}{\partial \mathbf{q}_{a(m)}(t_2)}\right)\right. \\ &\quad \left.\times\left(\frac{1}{k_BT}\dot{\mu}_j(t_1)\mu_i(t_0) - \left(\sum_m\sum_{b(n)}\frac{\partial\mu_j(t_1)}{\partial \mathbf{q}_{b(n)}(t_1)}\cdot\frac{\partial\mu_i(t_0)}{\partial \mathbf{p}_{b(n)}(t_1)}\right)\right)\right\rangle \\ &= \frac{1}{k_BT}\left\langle \sum_{i,j,k,l} w_{ijkl}(\tau_3,\tau_2,\tau_1)\right\rangle, \end{aligned} \tag{12}$$

where i,j,k,l,m,n denote the molecules, and $a(m)$ denotes atom a in molecule m. By inserting the truncating function (7), the generating response function (10) becomes

$$W^{(4)}(\tau_3,\tau_2,\tau_1) = \frac{1}{k_BT}\left\langle \sum_{i,j,k,l}\left(w_{ijkl}(\tau_3,\tau_2,\tau_1)\prod_{\alpha,\beta=i,j,k,l,m,n} g_{\mathrm{t}}(\bar{r}_{\alpha\beta},r_{\mathrm{t}})\right)\right\rangle. \tag{13}$$

1.2 Stability matrix algorithm for classical response

Equation (12) contains two terms that involve derivatives of some quantities at one time with respect to a variable at another time. These can be recast using the chain rule as

$$\frac{\partial\alpha_l(t_3)}{\partial \mathbf{p}_{a(m)}(t_2)} = \sum_{m'}\sum_{a'(m')}\frac{\partial\alpha_l(t_3)}{\partial \mathbf{q}_{a'(m')}(t_3)}\cdot\frac{\partial \mathbf{q}_{a'(m')}(t_3)}{\partial \mathbf{p}_{a(m)}(t_2)}, \tag{14}$$

and

$$\frac{\partial\mu_i(t_0)}{\partial \mathbf{p}_{b(n)}(t_1)} = \sum_{n'}\sum_{b'(n')}\frac{\partial\mu_i(t_0)}{\partial \mathbf{q}_{b'(n')}(t_0)}\cdot\frac{\partial \mathbf{q}_{b'(n')}(t_0)}{\partial \mathbf{p}_{b(n)}(t_1)}. \tag{15}$$

Equations (14) and (15) represent forward (from t_2 to t_3) and backward (from t_1 to t_0) propagations. To compute these quantities, we introduce the *stability matrix* from time t to $t+\Delta t$

$$S(t+\Delta t,t) = \begin{pmatrix} \frac{\partial\mathbf{p}(t+\Delta t)}{\partial\mathbf{p}(t)} & \frac{\partial\mathbf{q}(t+\Delta t)}{\partial\mathbf{p}(t)} \\ \frac{\partial\mathbf{p}(t+\Delta t)}{\partial\mathbf{q}(t)} & \frac{\partial\mathbf{q}(t+\Delta t)}{\partial\mathbf{q}(t)} \end{pmatrix}. \tag{16}$$

We now consider the propagation of the stability matrix from time t to $t+2\Delta t$. The time-evolution of the stability matrix can be calculated as

$$\frac{\partial\mathbf{p}(t+2\Delta t)}{\partial\mathbf{p}(t)} = \frac{\partial\mathbf{p}(t+2\Delta t)}{\partial\mathbf{p}(t+\Delta t)}\cdot\frac{\partial\mathbf{p}(t+\Delta t)}{\partial\mathbf{p}(t)} + \frac{\partial\mathbf{p}(t+2\Delta t)}{\partial\mathbf{q}(t+\Delta t)}\cdot\frac{\partial\mathbf{q}(t+\Delta t)}{\partial\mathbf{p}(t)}. \tag{17}$$

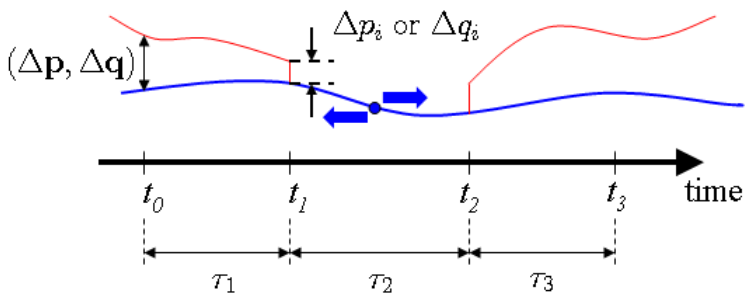

Figure 2: Schematic representation of the MD protocol for calculating the fourth-order signal based on the stability matrix formalism. From the blue circle, the forward and backward MD runs are performed to calculate the stability matrix. Blue; the trajectory of the MD simulation. Red; the trajectories after the displacement of momentum (Δp_i) or position (Δq_i) of atom i.

When Equation (17) is applied for each element of the stability matrix, we obtain[6, 7]

$$S(t + 2\Delta t, t) = S(t + 2\Delta t, t + \Delta t)S(t + \Delta t, t). \tag{18}$$

The stability matrix can be conveniently propagated in time by using Equation (18).

1.3 Molecular Dynamics (MD) simulations

MD simulations start at $t = 0$. Both forward (from $t = 0$ to $t = t_3$) and backward (from $t = 0$ to $t = t_1$) MD runs are carried out. The MD procedure is schematically drawn in Figure 2. The computation of the 2D IR (2D Raman) response functions based on the direct evaluation of four-point correlation functions requires $12N$ ($6N$) trajectories for the stability matrix in addition to equilibrium MD runs, where N is the number of atoms in a system. To achieve fast convergence of the response function, small systems have been used so far; 128 HF,[8] 64 water,[9] and 1 NMA solvated by 16 water[3] in classical or semiempirical/classical simulations for 2D IR response functions, and 32 Xe,[10] 32 CS_2,[11] and 108 formamides[12, 13] for the classical simulations of 2D Raman. Unlike the bulk systems used in these earlier studies, a relatively large number of molecules is required for modeling water/lipid structures. In the present study, the system consisted of 8 DMPC and 472 water molecules, which was ten times larger than the systems used in recently reported MD simulations of 2D IR spectra.[8, 9] To reduce computational cost, we made some additional approximations.

Large energy fluctuations in the microcanonical NVE ensemble strongly affect the stability matrix. To suppress these fluctuations, we must use a small time step, increasing the computational cost. MD

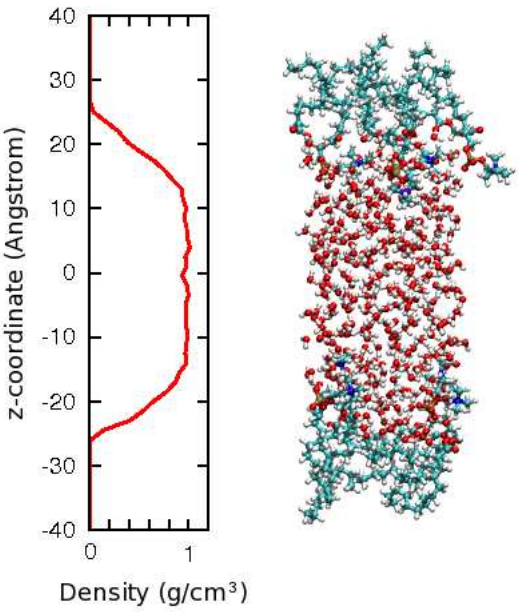

Figure 3: Left: Water density profile along the z-axis perpendicular to the interface. Right: Snapshot of the simulated water/DMPC interface. Water and DMPC molecules are denoted in red and green colors, respectively.

simulations with a polarizable water model have larger energy fluctuations than a fixed charge model. We thus employed the non-polarizable force field of water developed by Marti *et al.*[14] instead of the polarizable force field.[1, 15, 16] For DMPC, we employed the CHARMM force field[17] without scaling the 1-4 intramolecular interactions. The reversible reference system propagator algorithm (r-RESPA)[18] was used to accelerate the MD simulation. A short time step of 0.05fs was used for integrating the equations of motion for the intramolecular interactions, while a longer time step of 0.5fs was used for the intermolecular interactions. The Coulombic sums were calculated by using the Wolf method with $\alpha = 0.1\text{Å}^{-1}$ and $r_c = 9.0\text{Å}$.[19, 20]

The initial equilibrated structure of the water/DMPC interface was taken from Ref. [21] . We randomly selected 8 DMPC molecules from the eqilibrated structure and put them in the cell. The cell size was 18.6Å in the interfacial plane x- and y-dimensions and 120Å in the perpendicular z-dimension. The system was solvated by 462 water molecules. We generated three independent snapshots. For these samples, the 0.4ns MD run was performed at 360K for randomizing the systems, and then 0.6ns MD run was carried out for cooling down the systems to 300K by using the velocity rescaling. We then ran the MD simulations for 1ns in the NVE ensemble for equilibrating the systems. The water profile and a typical snapshot are given in 3. From the 3ns production MD run, we harvested over 78000 snapshots. For each snapshot, we performed the forward and backward MD runs for 300 MD steps (150fs). The stability matrix was calculated every 3 MD steps (1.5fs).

A large system requires not only a long simulation time for each snapshot but extensive sampling, because the the cross-correlations of distantly positioned molecules show large fluctuations in a finite time as discussed above. To reduce cost, we neglected the intermolecular cross-correlation contribution by setting $r_t = 0$ in Equation (7). The same approximation was employed in Ref. [3]. The dipole moment and polarizability are given by the sum of the permanent and induced terms

$$\mu_i'(t) = \mu_i^{\mathrm{perm}}(t) + \mu_i^{\mathrm{ind}}(t), \tag{19}$$

$$\alpha_i'(t) = \alpha_i^{\mathrm{perm}}(t) + \alpha_i^{\mathrm{ind}}(t). \tag{20}$$

The permanent dipole moment and polarizability were calculated following Ref. [22]. The induced dipole and polarizability were calculated in the first-order dipole-induced dipole model

$$\mu_i^{\mathrm{ind}} = \sum_j \left(\frac{\mu_j^{\mathrm{perm}} \alpha_i^{\mathrm{perm}}}{r_{ij}^3} - \frac{3\left(\mu_j^{\mathrm{perm}} \mathbf{r}_{ij}\right) \cdot \left(\mathbf{r}_{ij} \alpha_i^{\mathrm{perm}}\right)}{r_{ij}^5} \right) g_1(r_{ij}), \tag{21}$$

and

$$\alpha_i^{\mathrm{ind}} = \sum_j \left(\frac{\alpha_j^{\mathrm{perm}} \alpha_i^{\mathrm{perm}}}{r_{ij}^3} - \frac{3\left(\alpha_j^{\mathrm{perm}} \mathbf{r}_{ij}\right) \cdot \left(\mathbf{r}_{ij} \alpha_i^{\mathrm{perm}}\right)}{r_{ij}^5} \right) g_1(r_{ij}). \tag{22}$$

The screening function

$$g_1(r) = \begin{cases} 1 & \text{for} \quad r < 0.8 r_c \\ 1 - 10x^3 + 15x^4 - 6x^5 & \text{for} \quad 0.8 r_c < r < r_c \\ 0 & \text{for} \quad r_c < r \end{cases} \tag{23}$$

was used, where $x = 5r/r_c - 4$.

To reduce the noise due to bulk water, we introduced the screening function for the dividing surface as

$$g_{\mathrm{ds}}(z) = \mathrm{sgn}(z) \begin{cases} 1 & \text{for} \quad z_{\mathrm{ds}} + a < |z| \\ \frac{1}{2} \sin \frac{\pi(z - z_{\mathrm{ds}})}{2a} + \frac{1}{2} & \text{for} \quad z_{\mathrm{ds}} - a < |z| \leq z_{\mathrm{ds}} + a \\ 0 & \text{for} \quad |z| \leq z_{\mathrm{ds}} - a \end{cases}, \tag{24}$$

where $z_{\mathrm{ds}} = 13$Å and $a = 1$Å represent the z-coordinate of the dividing surface and the width of the screening region, respectively.[1] The dipole moment and polarizability are given by

$$\mu_i(t) = \mu_i'(t) g_{\mathrm{ds}}(z_i), \tag{25}$$

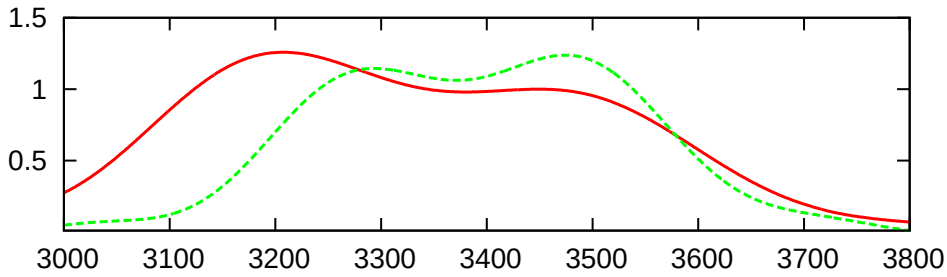

Figure 4: Heterodyne-detected SFG signals, $\mathrm{Im}(R^{(2)}_{xxz}(\omega))$. Red; simulation by using non-polarized water model. Green; previous polarizable force field simulation.[1]

and

$$\alpha_i(t) = \alpha'_i(t) g_{\mathrm{ds}}(z_i)^2. \tag{26}$$

2 Simulations of SFG Spectra

The simulated SFG spectrum, $R^{(2)}_{xxz}(\omega)$ using a non-polarizable water model[14] is compared with the earlier polarizable water in Figure 4.[1, 16, 15] Both show two peaks at 3100-3300 and 3300-3500cm^{-1}. The red-shifted peak simulated in the current study is stronger than the blue-shifted peak, whereas the intensities of both peaks are similar in the previous study. In addition, the frequency of the red-shifted peak in this study is lower than the previous simulation.

Interfacial water is oriented to DMPC due to the strong electrostatic potential of the negatively charged part of DMPC,[1] and the screening effect due to the induced dipole moment of water weakens the electrostatic interaction with DMPC in the interfacial region. Since the electrostatic potential generated by DMPC is not screened by non-polarizable water model but is disturbed by the fixed charges of water which are optimized for describing bulk water properties, it is overestimated in the non-polarizable water model. This makes the ordered structures of interfacial water, causing larger red-shifted peak.

References

[1] Nagata, Y.; Mukamel, S. *J. Am. Chem. Soc.* **2010**, 132, 6434-6442.

[2] Mukamel, S. *Principles of Nonlinear Optical Spectroscopy* (Oxford University Press, New York, 1995).

[3] Jeon, J.; Cho, M. *New J. Phys.* **2010**, 12, 065001.

[4] Nagata, Y.; Tanimura, Y. *J. Chem. Phys.* **2006**, 124, 024508.

[5] Nagata, Y.; Hasegawa, T.; Tanimura, Y. *J. Chem. Phys.* **2006**, 124, 194504.

[6] Mukamel, S.; Khidekel, V.; Chernyak, V. *Phys. Rev. E* **1996**, 53, R1.

[7] Saito, S; Ohmine, I. *J. Chem. Phys.* **1998**, 108, 240.

[8] Hasegawa, T.; Tanimura, Y. *J. Chem. Phys.* **2008**, 128, 064511.

[9] Yagasaki, T.; Saito, S. *J. Chem. Phys.* **2008**, 128, 154521.

[10] Ma, A.; Stratt, R. M. *J. Chem. Phys.* **2002**, 116, 4962-4971.

[11] Saito, S.; Ohmine, I. *Phys. Rev. Lett.* **2002**, 88, 207401.

[12] Hasegawa, T.; Tanimura, Y. *J. Chem. Phys.* **2006**, 125, 074512.

[13] Li, Y. L.; Huang, L.; Miller, R. J. D.; Hasegawa, T.: Tanimura, Y. *J. Chem. Phys.* **2008**, 128, 234507 (2008).

[14] Marti, J.; Padro, J. A.; Guardia, E. *J. Mol. Liq.* **1994**, 62, 17-31.

[15] Ishiyama, T.; Morita, A. *J. Phys. Chem. C* **2007**, 111, 721-737.

[16] Nagata, Y. *ChemPhysChem* **2010** 11, 474-479.

[17] Klauda, J. B.; Brooks, B. R.; MacKerell, A. D. Jr.; Venable, R. W.; Pastor, P. W.; *J. Phys. Chem. B* **2005**, 109, 5300-5311.

[18] Tuckerman, M.; Berne, B. J.; Martyna, G. J. *J. Chem. Phys.* **1992**, 97, 1990-2001.

[19] Wolf, D.; Keblinski, P.; Phillpot, S. R.; Eggebrecht, J. *J. Chem. Phys.* **1999**, 110, 8254-8282.

[20] Fennell, C. J.; Gezelter, J. *J. Chem. Phys.* **2006**, 124, 234104.

[21] http://terpconnect.umd.edu/∼jbklauda/research/download.html

[22] Morita, A.; Hynes, J. T. *J. Phys. Chem. B* **2002**, 106, 637-685.